Article

Design of a Wind Harvester to Complement the Power Supply of Remote Weather Stations

Alberto Pasetto , Gino Filipi , Michele Tonan , Manuele Bertoluzzo , Matteo Bottin , Daniele Desideri , Federico Moro , Alberto Doria *

Posted Date: 2 March 2026

doi: 10.20944/preprints202603.0015.v1

Keywords: Piezoelectric harvester; vibrations; wind excitation; galloping

Preprints.org (www.preprints.org) | NOT PEER-REVIEWED | Posted: 2 March 2026 doi:10.20944/preprints202603.0015.v1

Article

Design of a Wind Harvester to Complement the Power Supply of Remote Weather Stations

Alberto Pasetto, Gino Filipi, Michele Tonan, Manuele Bertoluzzo, Matteo Bottin, Daniele Desideri, Federico Moro and Alberto Doria*

Department of Industrial Engineering, University of Padova, 35131 Padova, Italy
* Correspondence: alberto.doria@unipd.it (A.D.); Tel.: +39-049-827-6803

Abstract

The possibility of exploiting wind-induced vibrations to harvest energy for the supply of remote weather stations is analyzed. Three kinds of wind-induced vibrations are considered: vortex induced vibrations, galloping and flutter. Experimental tests on prototypes and numerical results show that the galloping harvester is the most suited to the proposed application. The numerical model makes it possible to simulate both T-shaped and I-shaped harvesters and to analyze the effect of variations in the main design parameters: bluff-body mass, cantilever stiffness and damping. Experimental tests show that the T-shaped configuration is ss sensor for environmental monitoring, without need of a battery.

Keywords: Piezoelectric harvester; vibrations; wind excitation; galloping

---

1. Introduction

The present era is characterized by wide networks of sensors that monitor natural, industrial and urban environments and send data to mainframes for analysis, prediction and simulation. In many practical conditions wireless sensors are needed, since wiring is not feasible or is complex and expensive.

The simplest energy source for a remote sensor node is a battery, but batteries have high replacement costs and the disposal of used batteries poses environmental problems. Nowadays many wireless sensor nodes are equipped with solar panels. But the energy produced by solar panels in severe weather conditions and during night is sometimes not sufficient to feed the sensor node and solar panels are complemented by batteries that are characterized by the above-mentioned problems.

A smarter solution consists in complementing the solar panel with other devices able to harvest other forms of energy from the surrounding environment, such as kinetic energy from wind and water streams, heat, mechanical energy from vibrations [1]. In recent years, much research has been conducted to develop energy harvesting technologies [2,3]. Nowadays, mechanical energy harvesting devices based on piezoelectric, electromagnetic, and triboelectric technologies are available.

The main goal of this article is to design an energy harvester that can replace the battery of a remote weather station. Remote weather stations can be installed in very different locations ranging from home backyards to the summits of mountain or cliffs. Nevertheless, all these locations share the common feature of being exposed to wind and rain.

The impact of raindrops can produce a significant excitation [4,5] but in some areas rainfalls are scarce in some seasons. Conversely, wind represents a more constant and widespread source of energy. For this reason this paper focuses on wind excitation. Modern energy harvesting technologies make it possible to collect wind energy without making use of rotary equipment, with great advantages in terms of simplicity of design. These harvesters exploit self-sustained vibrations generated by wind and convert mechanical vibration energy into useful electric energy exploiting piezoelectric, electromagnetic and triboelectric phenomena. The piezoelectric harvesters are particularly suited to this application, since they have a large electro-mechanical coupling coefficient and the integration layers of piezoelectric material with the vibrating structure is rather easy and cost-effective.

The piezoelectric materials, the harvesters layouts and the experimental equipment used in this research are presented in Section 2.

An elastically suspended body impacted by a constant wind may experience different kinds of self-sustained vibrations depending on its geometry and on the characteristics of the suspension system that can let one or more degrees of freedom (DOFs) to the vibrating body. For this reason, different kinds of piezoelectric harvesters based on vortex induced vibrations (VIV) [6,7], galloping [8,9] and flutter [10,11] have been developed and tested.

The application of wind harvesters (WH) to remote weather stations is not characterized by very stringent constraints in terms of harvester geometry, weight, and encumbrance, but WH must comply with the low input voltage of IoT system electronics and must generate adequate power at the same time. In the scientific literature, there are not many studies that address the comparison between different types of WH from the perspective of a specific application. Therefore, Section 3 makes a comparison between a VIV, a galloping and a flutter harvester having similar dimensions with the aim of finding the harvester configuration that is more suited to complement solar panels in remote weather stations.

Since Section 3 shows that the galloping harvester is the best choice for this applications, in Section 4 a mathematical model of galloping harvester is developed and validated. Then in Section 5 the mathematical model and experimental tests are used to refine the mechanical design of the galloping harvester. In particular, since in the scientific literature there are not many comparisons between T- and I-shaped galloping harvesters, the two configurations are analyzed considering some constraints that are relevant to the present application. Section 6 considers as a target load electrical power an electrical load, the a typical IoT station Finally, conclusions are drawn in Section 7.

2. Materials and Experimental Setup

Weather stations typically measure a complete set of meteorological parameters such as temperature, humidity, wind, rain, UV, and light intensity. They have sizes of some hundreds of mm and weight of about 1 kg. This research focuses on a weather station located in the North East of Italy (near Padua). In this area the mean wind velocity is about 2 m/s with a maximum value of about 10 m/s.

Taking into account the above dimensions and environmental conditions, this research focuses on wind harvesters equipped with bluff bodies with maximum dimensions of about 200 mm and a reference area of about 3000 mm^2.

There are many kinds of flow induced vibrations than can be exploited by wind harvesters. They are related to the vibrational motion in a steady flow of an elastically suspended body. If the body is a cylinder, due to the symmetry of the cross section the aerodynamic coefficients do not vary with cylinder attitude and the resultant wind force is always parallel to the relative wind velocity; in this case vibrations are excited by the von Karman vortexes that in certain conditions are shed downstream the cylinder. The first harvesters based on vortex induced vibrations (VIV) were developed in [12–14] and details on the properties and design of these harvesters can be found in [6,15].

When the elastically suspended body has a more general cross section (e.g. square, triangle, half-cylinder) the aerodynamic coefficients change as the body vibrates in the flow and galloping self-sustained vibrations take place. The first studies on galloping harvesters was presented in [8,16] and details on the performance and design of these harvesters can be found in [17].

If the non-cylindrical body can perform two-degree-of-freedom vibrations including plunge and pitch, the dominant phenomenon becomes the flutter instability. The first flutter harvesters were presented in [10] and a review of the performances of these devices can be found in [18].

The common features of the above-mentioned wind harvesters can be summarized as follows:

- the aerodynamic force that fosters vibrations is proportional to the area of the vibrating body;
- the vibrating body is elastically suspended by means of a cantilever beam;

- vibrating body mass is light;
- the active piezoelectric layer is bonded on the surface of the cantilever.

Therefore, in the framework of this research plastic vibrating bodies with different shapes, but with the same reference area were adopted. They were manufactured using a 3D printer. All the tested harvesters were equipped with the same aluminum cantilever beam having a lenght of 130 mm and a rectangular cross-section of 21 × 1 mm. On the surface of the cantilever beam and near the clamp a piezoelectric patch M2814-P2 built by Smart material GmbH was glued. The active layer of this patch is made of MFC composite.

The prototype harvesters were tested in the wind tunnel depicted in Figure 1. The rectangular cross-section of the tunnel measures 190 mm in width and 200 mm in height. These dimensions guarantee that, when the prototypes are mounted inside the wind tunnel, the blockage effect is small [19] and there is a sufficient gap between the ends of the bluff-body and the walls of the wind tunnel [20]. The wind flow is generated by a fan that allows a maximum wind velocity of 6 m/s. Wind velocity was measured by means of a TSI 8455-300-1 air velocity transducer with accuracy of 2 % of reading.

The voltage generated by the harvester was measured by means of a National Instruments NI 9230 board and processed by a MATLAB code. Typical sampling rate and acquisition time were 2048 Hz and 10 s respectively.

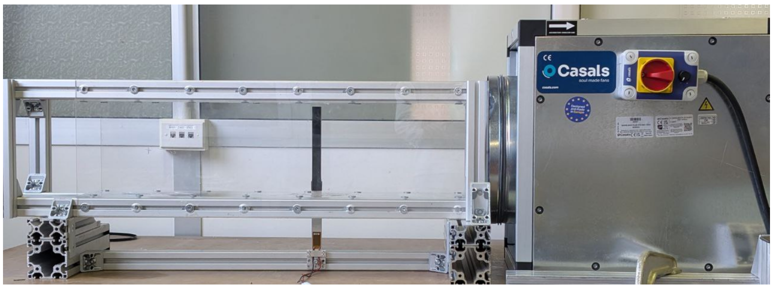

Figure 1. Wind tunnel with I-shaped galloping harvester

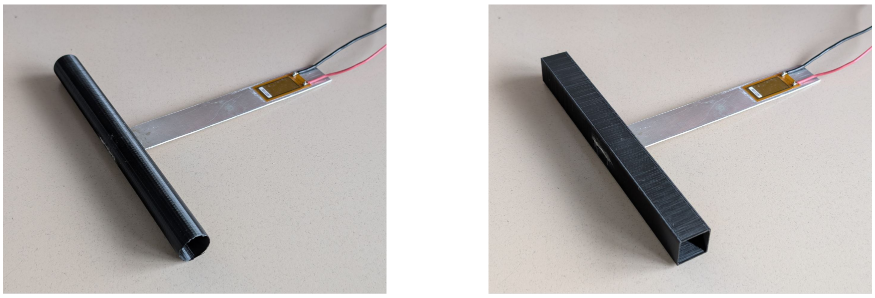

(**a**) (**b**)

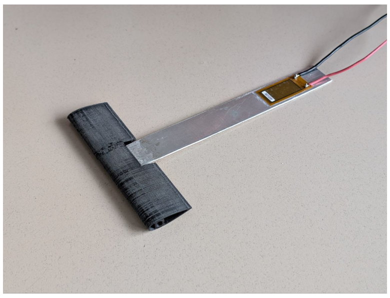

(**c**)

Figure 2. Piezoelectric energy harvester equipped with bluff-body to generate (a) vortex-induced vibration (VIV); (b) Galloping; and (c) Flutter

Preprints.org (www.preprints.org) | NOT PEER-REVIEWED | Posted: 2 March 2026 doi:10.20944/preprints202603.0015.v1

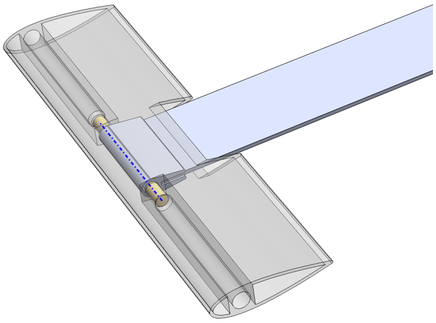

Figure 3. CAD model of the piezoelectric energy harvester equipped with bluff-body to generate flutter phenomena.

3. Choice of the Self-Excitation Mechanism

This section aims to make a comparison between T-shaped piezoelectric harvesters based on VIV, galloping and flutter. The T-shaped harvester features the vibrating body (excited by wind flow) perpendicular to the cantilever longitudinal axis and can be realized for the three kinds of harvesters. The harvester prototypes are shown in Figure 2, the CAD detail of the flutter harvester is depicted in Figure 3.

Wind harvesters based on VIV generate voltage exploiting the coincidence of the natural frequency with the frequency of vortex shedding from the cylindrical bluff-body. The basic equation for the design of the VIV harvester is:

$$f_n = \mathrm{St}\,\frac{U}{D} \tag{1}$$

where f_n is the natural frequency of the harvester and the term St $\frac{U}{D}$ is the vortex shedding frequency form a steady cylinder with diameter D and exposed to a wind flow having velocity U. St is the Strouhal number [21]. Actually the behavior of the vibrating cylinder is more complex, since vibrations affect the vortex shedding and a lock-in phenomenon takes place [22]. Nonetheless, Equation (1) is a good starting point for the design of the harvester. The prototype VIV harvester, which is depicted in Figure 2(**a**), was designed with $D = 19$ mm St $= 0.17$ and $U = 2$ m/s. With the aluminum cantilever described in the previous section and a tip mass $M = 0.008$ kg, the harvester natural frequency resulted $f_n = 18$ Hz.

Figure 4 depicts experimental results obtained with the prototype VIV harvester, whose geometric and mechanic parameters are reported in Table 1.

Table 1. Parameters of the harvesters.

Parameter	VIV	Galloping	Flutter
Cylinder diameter	19 mm	/	/
Section width	/	19 mm	/
Airfoil chord	/	/	30 mm
Bluff-body/Airfoil mass	0.008 kg	0.008 kg	0.010 kg
Bluff-body/Airfoil span	178 mm	178 mm	112 mm
Bluff-body/Airfoil moment of inertia *	1.5 kg mm^2	1.7 kg mm^2	0.7kg mm^2
Cantilever length	130 mm	130 mm	130 mm
Cantilever width	21 mm	21 mm	21 mm
Cantilever thickness	1 mm	1 mm	1 mm
Patch length	28 mm	28 mm	28 mm
Distance of the patch from the clamp	8 mm	8 mm	8 mm

* Moment of inertia around the cantilever tip.

Preprints.org (www.preprints.org) | NOT PEER-REVIEWED | Posted: 2 March 2026 doi:10.20944/preprints202603.0015.v1

The rms value of the open circuit (OC) voltage generated by the harvester is plotted against wind velocity. Each voltage value is the average of three different measurements.

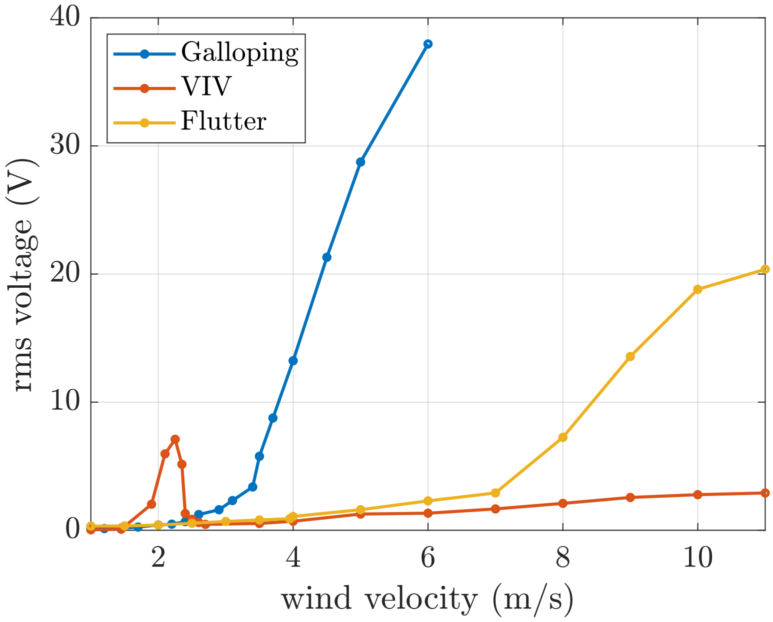

Figure 4. Experimental voltage generated exploiting different self-excitation mechanisms. The reference area of the aerodynamic body is fixed.

The VIV harvester is able to generate a relevant OC voltage (about 8 V) only when wind velocity reaches the value that makes the vortex shedding frequency equal to the harvester natural frequency. For lower or higher values of wind velocity the voltage generated by the harvester is very small, it slightly increases when wind increases due to the increased excitation due to turbulence.

The prototype galloping harvester was built simply by substituting the cylindrical bluff-body of the VIV harvester with a square section bluff-body having the same projected area and the same mass (see Figure 2(**b**)). Galloping vibrations are self-sustained vibrations that take place above a certain wind velocity (onset velocity U_G), when the fluctuating aerodynamic forces due to the variation in the aerodynamic coefficients cancel the mechanical damping forces (and, when the harvester is connected to an external electrical load, the mechanical and electrical damping forces). Above U_G the vibrating system experiences large amplitude oscillations that increase until a limit cycle is reached.

In open-circuit conditions the onset velocity of galloping vibrations [8,23] is given by the following formula:

$$U_G = \frac{2c_1}{a_1 \rho D L_T \sigma_1} \tag{2}$$

where c_1 is modal damping, ρ air density, D and L_T are the width and length of the bluff-body respectively, a_1 is an aerodynamic coefficient and σ_1 a constant related to the shape of the first mode of vibration of the harvester. With the selected geometric and mechanical properties of the prototype galloping harvester (which are summarized in Table 1) onset velocity U_G resulted 3.5 m/s. The measured values of the rms OC voltage generated by the prototype for increasing values of wind velocity are reported in Figure 4. The behavior of the galloping harvester is very different from the one of the VIV harvester, because the galloping harvester for wind velocities exceeding U_G generates a continuously increasing voltage that reaches the value of 37 V at 6 m/s. Larger values of wind velocity were not tested with this harvester, because already at 6 m/s vibration amplitude was very large.

Flutter vibrations are another kind of self-sustained vibrations, they are different from galloping vibrations because they take place in elastically suspended airfoils having at least two degrees of freedom: the plunge DOF and the pitch DOF. In the T-shaped harvester the flexibility of the cantilever gives the plunge DOF, whereas a revolute joint between the tip of the cantilever and the airfoil body allows the pitch DOF. The presence of a torsion spring around the pitch axis is not mandatory. There are some designs that include the torsion spring [24] and some designs that do not include the torsion spring [25]. Generally speaking, the design of a T-shaped flutter harvester is more complex than the design of the other harvesters, since the revolute joint has to be accommodated inside the small thickness of the airfoil.

The flutter harvester prototype was developed starting from a 0024 NACA profile with a mass of 10 g (see Figure 2(**c**)). Since standard NACA profiles have a fixed ratio between the maximum thickness and chord length, the chord length was increased to obtain a sufficient room for the revolute joint. In order to keep the airfoil area equal to the ones of the VIV and galloping harvesters, the length of the flutter harvester was accordingly decreased.

The layout of the revolute joint is depicted in Figure 3. A plastic sleeve fitted with two cylindrical pins was manufactured. Then, the sleeve was inserted and glued onto the end of the cantilever. Two cylindrical holes were made in the body of the airfoil. The revolute joint was obtained coupling the pins on the sleeve with the holes in the airfoil. Since in the present research simplicity and robustness of the harvesters are key issues, no torsion spring was inserted into the joint. The geometric and mechanical properties of the flutter harvester prototype are summarized in Table 1.

Flutter self-sustained vibrations take place if wind velocity becomes larger than a specific value, which is named flutter velocity. At the flutter velocity the device becomes dynamically unstable, large oscillations occur and amplitude increases until a limit cycle is reached. The complete study of a flutter harvester requires non-linear analysis methods [24,26], nevertheless, the onset of flutter instability can be studied numerically calculating the complex eigenvalues of a linearized system. A widely adopted linear model of a flutter harvester includes the lumped-parameter model of plunge and pitch vibrations and aerodynamic forces calculated according to the Theodorsen's unsteady thin airfoil theory [10]. Some preliminary calculations carried out with this method showed that the designed airfoil becomes unstable for wind velocities larger than 6.3 m/s. Then the designed flutter harvester was tested in the wind tunnel. Figure 4 reports experimental results in terms of rms OC voltage versus wind velocity. The trend of the OC voltage generated by the flutter harvester is similar to the one of the galloping harvester, but the flutter velocity is larger than the galloping velocity and the slope is lower.

Finally, the comparison between the three harvester prototypes highlights that the best choice for the power supply of a weather station operating in a low wind region is the galloping harvester, provided that the galloping velocity can be a bit lowered.

The VIV harvester exhibits good performances at the design wind velocity (lock-in condition), but it works well only for a very narrow range of wind velocities about the lock-in value. It is safer than the other harvesters in severe weather conditions, because if wind velocity is large, but outside the lock-in value, the amplitude of vibrations is small.

The flutter harvester is more complex than the galloping harvester, its design is complex, since there is no analytical expression of flutter velocity. The flutter velocity is larger than the galloping velocity.

For the above mentioned reasons, the rest of the paper will deal with galloping harvesters focusing on design solutions suited to lower the galloping onset velocity.

4. Mathematical Model of the Galloping Harvester

The T-shaped harvester considered in the previous section is the simplest layout of a galloping harvester. But with the same elements (cantilever, piezoelectric patch, and bluff-body) a I-shaped harvester can be built with the bluff-body axis aligned with the longitudinal axis of the cantilever (see Figure 5). From the point of view of lowering galloping onset velocity U_G, the I layout is promising, since the moment of inertia of the bluff-body with respect to the cantilever end point strongly increases leading to large variations in the parameters that appear in Equation (2). Therefore, the mathematical model of the galloping harvester is developed with the aim of modeling both T-shaped and I-shaped harvesters.

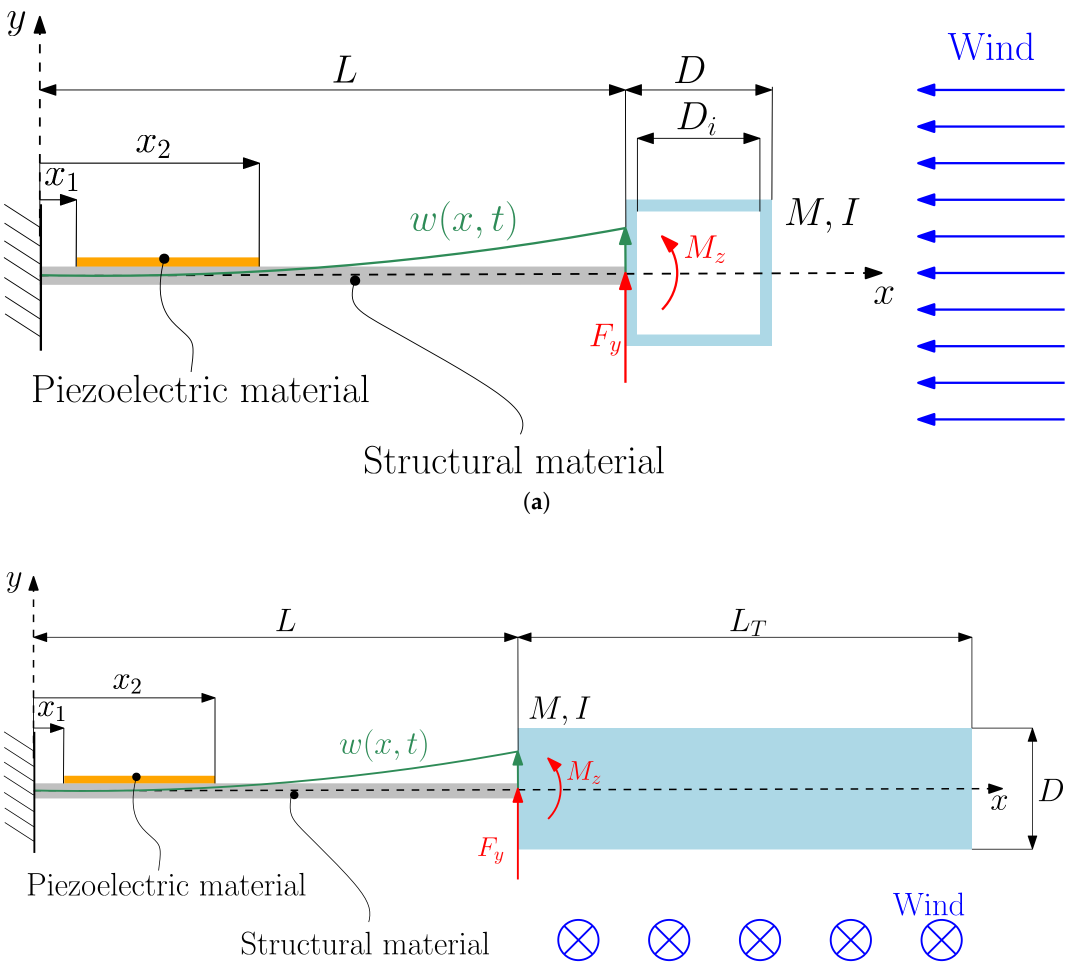

(**a**)

(**b**)

Figure 5. (a) Galloping T-shaped harvester; (b) Galloping I-shaped harvester.

The piezoelectric cantilever can be modeled as a continuous system, and forced vibrations are governed by the following partial differential equation:

$$\begin{aligned} &EJ\frac{\partial^4 w(x,t)}{\partial x^4} + E^* J\frac{\partial^5 w(x,t)}{\partial x^4 \partial t} + m\frac{\partial^2 w(x,t)}{\partial t^2} + c_a\frac{\partial w(x,t)}{\partial t} + \\ &\theta\, v(t)\left[\frac{d\delta(x-x_1)}{dx} - \frac{d\delta(x-x_2)}{dx}\right] = F_y(t)\delta(x-L) + M_z(t)\frac{d\delta(x-L)}{dx} \end{aligned} \tag{3}$$

where the spatial coordinate x identifies any point along the cantilever, and t corresponds to time. The function $w(x,t)$ describes the transverse displacement measured from the undeformed shape of the cantilever. The bending stiffness is given by EJ, where J is the equivalent area moment of inertia, and E^* is the Kelvin-Voigt time-independent viscoelastic constant, c_a is the viscous damping coefficient of the beam related to air damping, m denotes the mass per unit length of the beam, and δ represents the Dirac delta function. The term $v(t)$ denotes the voltage, and θ represents the piezoelectric coupling term and is defined as:

$$\theta = \frac{e_{31}\, b}{2\, h_p}\left(h_b^2 - h_c^2\right) \tag{4}$$

where e_{31} is the piezoelectric constant, b is the width of the piezoelectric patch, h_p denotes the thickness, and h_b and h_c define the distances from the neutral axis to the bottom and top surfaces of the piezoelectric layer, respectively.

At the right-hand side of Equation (3) there are the forcing term related to the aerodynamic excitation, in particular $F_y(t)$ represents the lumped aerodynamic force due galloping phenomena applied to the end of the cantilever beam, whereas $M_z(t)$ is the torque generated by the force acting on the bluff-body reported at the end of the cantilever.

The transverse displacement $w(x,t)$ can be expressed by means of the modal expansion approach:

$$w(x,t) = \sum_{m=1}^{\infty} \Psi_m(x)\eta_m(t) \tag{5}$$

where $\Psi_m(x)$ is the mth mode of vibration and $\eta_m(t)$ is the mth modal displacement. The mode of vibration are normalized such that $\Psi_m(L) = 1$.

The modal equations of the cantilever harvester can be obtained by introducing Equation (5) into Equation (3) and exploiting the orthogonality properties of the modes of vibration:

$$\begin{aligned} &m_n \frac{d^2\eta_n(t)}{dt^2} + c_n \frac{d\eta_n(t)}{dt} + k_n\eta_n(t) + \varphi_n v(t) = F_y(t)\Psi_n(L) + M_z(t)\Psi_n^{'}(L) \\ &\text{with } n = 1, \dots, \infty \end{aligned} \tag{6}$$

The term φ_n represent the backward modal coupling term of the nth mode of vibration and it is defined as:

$$\varphi_n = \theta \left(\left. \frac{d\Psi_n(x)}{dx} \right|_{x=x_2} - \left. \frac{d\Psi_n(x)}{dx} \right|_{x=x_1} \right) \tag{7}$$

The terms m_n, k_n and c_n represent the modal mass, modal stiffness and modal damping of the system, respectively. They can are defined as follows:

$$m_n = \int_0^L \Psi_n(x)\, m\Psi_n(x)\, dx + M\Psi_n(L)^2 + 2p\Psi_n(L)\Psi_n^{'}(L)M + \left. \frac{d\Psi_n(x)}{dx} \right|_{x=L} I \left. \frac{d\Psi_n(x)}{dx} \right|_{x=L} \tag{8}$$

$$k_n = \int_0^L \frac{d^2\Psi_n(x)}{dx^2} EJ \frac{d^2\Psi_n(x)}{dx^2} dx \tag{9}$$

$$c_n = 2\zeta_n \sqrt{k_n m_n} \tag{10}$$

where ζ_n is the modal damping ratio of the n-th vibration mode, p is the distance between the cantilever end and the center of mass of the bluff-body, I is the moment of inertia of the bluff-body calculated with respect to the end of the cantilever. The variables p and I are defined as follows:

$$p = \begin{cases} \dfrac{D}{2} \\ \\ \dfrac{L_T}{2} \end{cases}, \quad I = \begin{cases} \dfrac{1}{6}M(D^2 + D_i^2) + M\dfrac{D^2}{4} & \text{for T-shaped harvester} \\ \\ \dfrac{1}{12}M(D^2 + D_i^2 + L_T^2) + M\dfrac{L_T^2}{4} & \text{for I-shaped harvester} \end{cases} \tag{11}$$

According to the approach presented in [27], the voltage generated by the piezoelectric cantilever is obtained as follows:

$$C_p\dot{v}(t) + i(t) = \sum_{m=1}^{\infty} \varphi_m\dot{\eta}_m(t) \tag{12}$$

where C_p represents the capacitance of the piezoelectric layer and $i(t)$ is the current flowing in the external load. The OC voltage can be obtained by integrating Equation (12), with $i(t) = 0$, yielding:

$$v(t) = v_0 + \frac{1}{C_p} \sum_{m=1}^{\infty} \varphi_m\eta_m(t) \tag{13}$$

where v_0 is the initial OC voltage. At this point, Equation (13) can be introduced into Equation (6) by considering $v_0 = 0$:

$$m_n \frac{d^2\eta_n(t)}{dt^2} + c_n \frac{d\eta_n(t)}{dt} + k_n\eta_n(t) + \varphi_n \frac{1}{C_p} \sum_{m=1}^{\infty} \varphi_m \eta_m = F_y \Psi_n(L) + M_z \Psi_n'(L) \qquad \text{with } n = 1, \dots, \infty \tag{14}$$

In general, the electrical output of most cantilever energy harvesters arises primarily from the excitation of their first bending mode [7]. Hence, Equation (14) can be particularized by considering only the first mode ($n = 1$):

$$m_1 \frac{d^2\eta_1(t)}{dt^2} + c_1 \frac{d\eta_1(t)}{dt} + k_1\eta_1(t) + \frac{\varphi_1^2}{C_p}\eta_1 = F_y \Psi_1(L) + M_z \Psi_1'(L) \tag{15}$$

4.1. Force Due to Galloping - T-Shaped Harvester

The galloping instability stems from the body's transverse vibrations, which continuously alter the effective angle of attack between the structure and the approaching wind (see Figure 6). The resulting modifications in the aerodynamic lift and drag forces are expressed through the following equations:

$$F_D(t) = \frac{1}{2}\rho D L_T U_{rel}^2 C_D(\alpha) \tag{16}$$

$$F_L(t) = \frac{1}{2}\rho D L_T U_{rel}^2 C_L(\alpha) \tag{17}$$

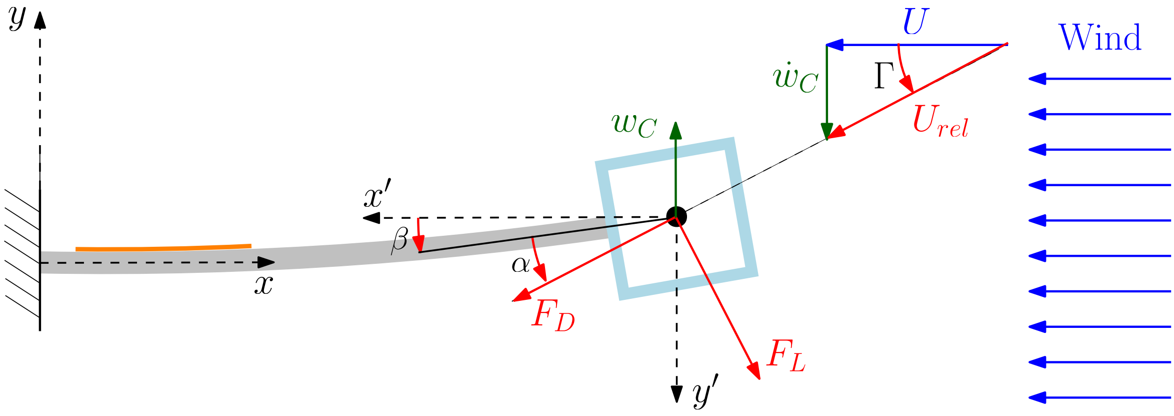

Figure 6. Angle of attack and aerodynamic forces.

The bluff-body is installed at the free end of the cantilever; consequently, the angle of attack varies due to two concurrent effects: the change in the cantilever's end slope produced by bending, and the change in the direction of the relative flow induced by the translational motion of the bluff-body. To formalize the definition of the angle of attack, a Cartesian coordinate system $x'y'z'$ must be introduced. The origin is located at the center of the bluff-body, and the x'-axis is always aligned with the incoming wind velocity U. When the cantilever deflects, the chord of the bluff-body forms an angle β with x':

$$\beta = \left.\frac{\partial\, w(x,t)}{\partial x}\right|_{x=L} \tag{18}$$

As shown in Figure 6, the relative velocity U_{rel} is rotated by the angle Γ with respect to the incoming wind velocity U. If the small oscillation hypothesis is considered, the angle Γ is given by the following equation:

$$\Gamma \approx \frac{\dot{w}_C}{U} = \frac{1}{U}\left(\left.\frac{\partial w(x,t)}{\partial t}\right|_{x=L} + \frac{D}{2} \left.\frac{\partial^2\, w(x,t)}{\partial x \partial t}\right|_{x=L} \right) \tag{19}$$

The angle of attack can be defined as the difference between the change in the cantilever's end slope and the change in the direction of the relative velocity, the following equation holds:

$$\alpha = \Gamma - \beta \tag{20}$$

Equation (20) can be rewritten by introducing the Equations (19) and (18):

$$\alpha = \frac{1}{U}\left(\frac{\partial w(x,t)}{\partial t}\bigg|_{x=L} + \frac{D}{2}\frac{\partial^2 w(x,t)}{\partial x \partial t}\bigg|_{x=L} \right) - \frac{\partial w(x,t)}{\partial x}\bigg|_{x=L} \tag{21}$$

If the modal expansion is introduced and only the first mode of vibration is considered (i.e. $n = 1$), Equation (21) becomes:

$$\alpha = \frac{1}{U}\left(\Psi_1(L)\dot{\eta}_1 + \frac{D}{2}\Psi_1'(L)\dot{\eta}_1 \right) - \Psi_1'(L)\eta_1 \tag{22}$$

The force $F_y(t)$, which appear in Equation (3), can be derived as described in [8] by projecting the lift and drag forces onto the y axis of the xyz frame:

$$F_y(t) = \frac{1}{2}\rho D L_T U^2 \left(a_1\alpha + a_3\alpha^3 \right) \tag{23}$$

where a_1 is positive constant and a_3 is negative constant. The moment $M_z(t)$, which appears in Equation (3), can be calculated by multiplying the force $F_y(t)$ by the distance between the end of the cantilever and the center of the bluff-body ($D/2$):

$$M_z(t) = \frac{1}{4}\rho D^2 L_T U^2 \left(a_1\alpha + a_3\alpha^3 \right) \tag{24}$$

Equations (23) and (24) can be introduced in Equation (15):

$$m_1\,\ddot{\eta}_1 + c_1\,\dot{\eta}_1 + k_1\eta_1 + \frac{\varphi_1^2}{C_p}\eta_1 = \frac{1}{2}\rho D L_T U^2 \left(a_1\alpha + a_3\alpha^3 \right)\left(\Psi_1(L) + \frac{D}{2}\Psi_1'(L) \right) \tag{25}$$

Substituting Equation (22) in Equation (25) and isolating the terms multiplied by $\dot{\eta}_1$, a linear equivalent damping can be found:

$$c_{eq} = c_1 - \frac{1}{2}a_1\rho D L_T U \left(\Psi_1(L) + \frac{D}{2}\Psi_1'(L) \right)^2 \tag{26}$$

Then, the onset velocity of galloping (U_G) can be found imposing $c_{eq} = 0$:

$$U_G = \frac{2c_1}{a_1\rho D L_T \left(\Psi_1(L) + \frac{D}{2}\Psi_1'(L) \right)^2} \tag{27}$$

In this configuration σ_1 of Equation (2) is:

$$\sigma_1 = \left(\Psi_1(L) + \frac{D}{2}\Psi_1'(L) \right)^2 \tag{28}$$

Equation (25) is numerically solved in MATLAB using the `ode45` solver for nonstiff differential equations.

The numerical model is used to estimate the OC voltage generated by the harvester for various values of wind velocity U.

The parameters a_1 and a_3 were retrieved from the experimental measurements obtained in Section 3. The rms of the OC voltage predicted by the model and the experimental measurements (mean value and standard deviation) are reported in Figure 7. Both the numerical model and the experimental measurements show a low voltage at wind velocity below 3.5 m/s. Above this velocity the system becomes unstable and the voltage increases with wind velocity.

The model is able to predict the galloping phenomenon observed in the experiments and makes it possible to extend the results to higher wind velocities. Below the galloping velocity, the experimental voltage is larger than the numerical voltage because of turbulence.

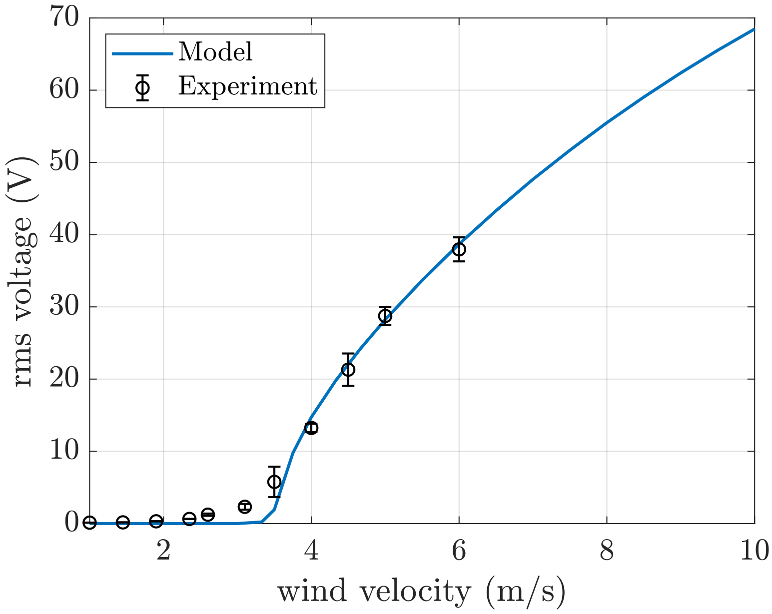

Figure 7. Voltage generated by the T Galloping harvester, ($a_1 = 1.9$, $a_3 = -16$)

4.2. Force Due to Galloping - I-Shaped Harvester

In the I configuration, the transverse velocity of the bluff-body $\dot{w}_C(\xi)$ varies along its span owing to the rotation of the tip β (see Figure 8).

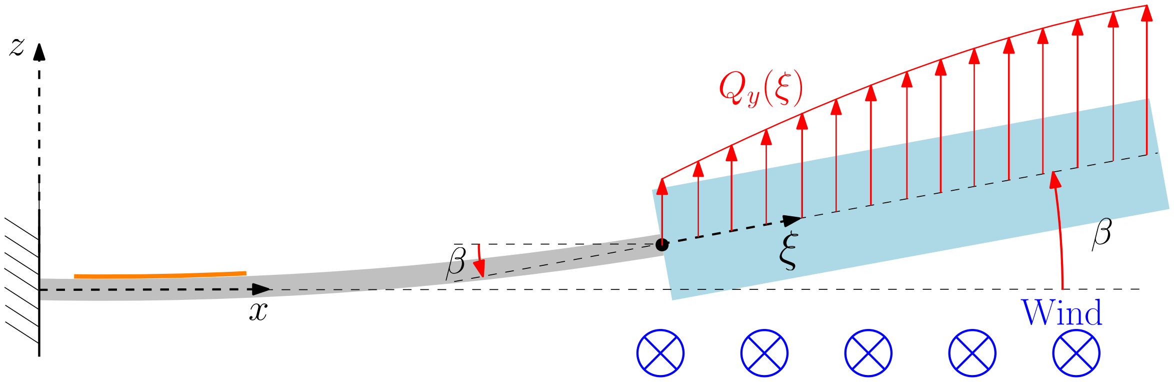

Figure 8. Angle of attack and aerodynamic load.

Therefore, the angle of attack and the aerodynamic load Q_y are not constant along the bluff-body. Introducing a spanwise coordinate ξ with its origin at the cantilever tip and assuming that the bluff-body rotates rigidly with the cantilever tip, the transverse velocity of the bluff-body is as follows:

$$\dot{w}_C(\xi) = \left.\frac{\partial w(x,t)}{\partial t}\right|_{x=L} + \xi \left.\frac{\partial^2 w(x,t)}{\partial x \partial t}\right|_{x=L} \tag{29}$$

and, for small amplitude vibrations, the angle of attack is:

$$\alpha(\xi,t) = \Gamma(\xi) \approx \frac{1}{U}\left(\left.\frac{\partial w(x,t)}{\partial t}\right|_{x=L} + \xi \left.\frac{\partial^2 w(x,t)}{\partial x \partial t}\right|_{x=L} \right) \tag{30}$$

Preprints.org (www.preprints.org) | NOT PEER-REVIEWED | Posted: 2 March 2026 doi:10.20944/preprints202603.0015.v1

Introducing Equation (5) in (30) and considering only the first mode of the beam:

$$\alpha(\xi,t) = \frac{1}{U}\left(\Psi_1(L)\dot{\eta}_1 + \xi\Psi_1'(L)\dot{\eta}_1\right) \tag{31}$$

Each section at a distance ξ from the cantilever tip is subjected to an aerodynamic load per unit length given by:

$$Q_y(\xi,t) = \frac{1}{2}\rho D U^2\left(a_1\,\alpha(\xi,t) + a_3\,\alpha^3(\xi,t)\right) \tag{32}$$

Finally, the resulting force F_y and torque M_z acting on the tip are obtained by the integration of the aerodynamic load:

$$F_y(t) = \int_0^{L_T} Q_y(\xi,t)\,\mathrm{d}\xi = \frac{1}{2}\rho D U^2\left(a_1\int_0^{L_T}\alpha(\xi)\,\mathrm{d}\xi + \ a_3\int_0^{L_T}\alpha^3(\xi)\,\mathrm{d}\xi\right) \tag{33}$$

$$M_z(t) = \int_0^{L_T}\xi\,Q_y(\xi,t)\,\mathrm{d}\xi = \frac{1}{2}\rho D U^2\left(a_1\int_0^{L_T}\alpha(\xi)\xi\,\mathrm{d}\xi + \ a_3\int_0^{L_T}\alpha^3(\xi)\xi\,\mathrm{d}\xi\right) \tag{34}$$

As for the T-shaped harvester, the onset velocity of galloping can be found by equating the equivalent linear damping to zero:

$$U_G = \frac{2c_1}{a_1\rho D L_T\left(\left(\Psi_1(L) + \frac{D}{2}\Psi_1'(L)\right)^2 + \frac{L_T^2}{12}\Psi_1'(L)\right)} \tag{35}$$

In this configuration σ_1 of Equation (2) is:

$$\sigma_1 = \left(\Psi_1(L) + \frac{D}{2}\Psi_1'(L)\right)^2 + \frac{L_T^2}{12}\Psi_1'(L) \tag{36}$$

Equations (33) and (34) can be introduced in Equation (15), and then solved in MATLAB using the `ode45` solver.

In order to adjust the parameters a_1 and a_3, the I-shaped harvester was tested in the wind tunnel. Figure 9 shows the experimental and numerical voltage generated by the harvester at various wind velocity.

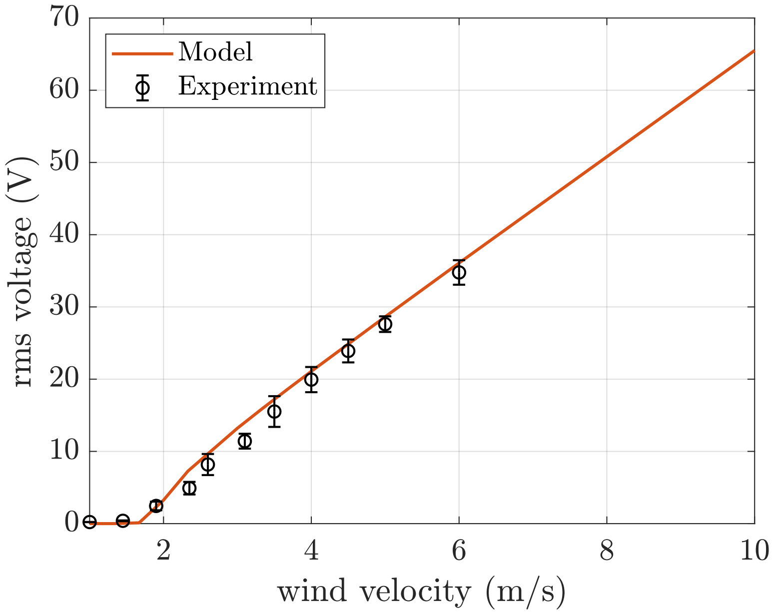

Figure 9. Voltage generated by the I Galloping harvester, ($a_1 = 1.7$, $a_3 = -120$).

As in the case of the T-shaped harvester, the voltage is almost zero below the onset galloping velocity and then it continuously increases. The onset galloping velocity is lower compared to the T-shaped harvester. Indeed, the voltage sharply grows above 2 m/s.

There is a good agreement between numerical and experimental results.

5. Numerical Simulations

The model presented and validated in Section 4 is used to investigate the effects of the main parameters of the galloping harvester: the tip mass M, the modal stiffness k_1, and the modal damping c_1. It is worth noticing that, owing to the normalization of $\Psi(x)$ adopted in this paper, the modal coordinate $\eta_1(t)$ represents the displacement of the tip and k_1 and c_1 represent the reduced stiffness and damping of the cantilever. The numerical investigation was carried out by varying one parameter at a time starting from the nominal values (M^*, k_1^*, and c_1^*) used in Sections 3 and 4. The analysis presented in this section is limited to harvesters with square section. The effect of different bluff-body shapes (triangle, funnel) was extensively studied in [23].

First, the effect of the tip mass was analyzed. The mass (M) was varied by changing the thickness of the bluff body and the moment of inertia I was calculated accordingly (see Equation (11)). The voltage generated by the T and I harvesters when the tip mass is changed by 20% from the nominal value is shown in Figure 10. The variation of tip mass does not affect the onset velocity of galloping; indeed, it does not appear directly in Equations (27) and (35), and has a negligible effect on the term $\Psi_1'(L)$. Above the onset velocity, the voltage is higher when a larger tip mass is used.

Then, the stiffness k_1 was varied without changing the geometry of the cantilever beam. The numerical results describing the effect of stiffness are shown in Figure 11. The onset velocity of galloping does not change with k_1, which does not appear in Equations (27) and (35). Above the onset velocity, an higher voltage is obtained whit a smaller stiffness. It can be observed that reducing the stiffness or increasing the tip mass have similar effects.

Finally, the numerical results with different values of the damping coefficient c_1 are presented in Figure 12. The onset velocity of galloping varies with damping; indeed, U_G depends linearly on c_1 (see Equations (27) and (35)). When U_G changes, the voltage curve translates along the horizontal axis maintaining its slope. An harvester with smaller damping starts generating a relevant voltage at lower wind velocities and, at higher velocities, generates an higher voltage compared to harvesters with larger damping.

Variations in M, k_1, and c_1 have similar effects on the T- and I-shaped harvesters.

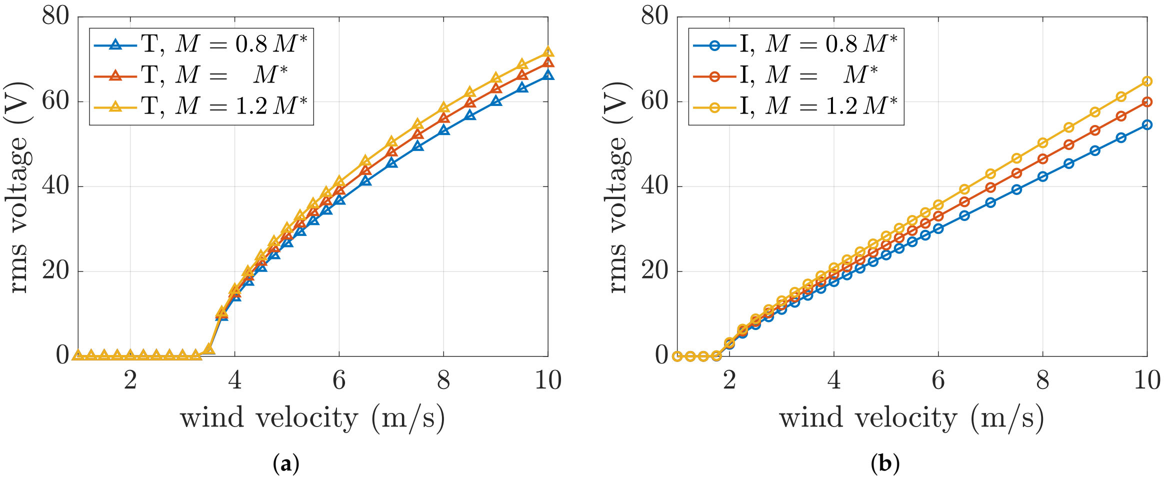

Figure 10. Effect of tip mass on the OC voltage generated by the "T" (**a**) and "I" (**b**) harvesters with fixed stiffness (k_1) and damping coefficient (c_1).

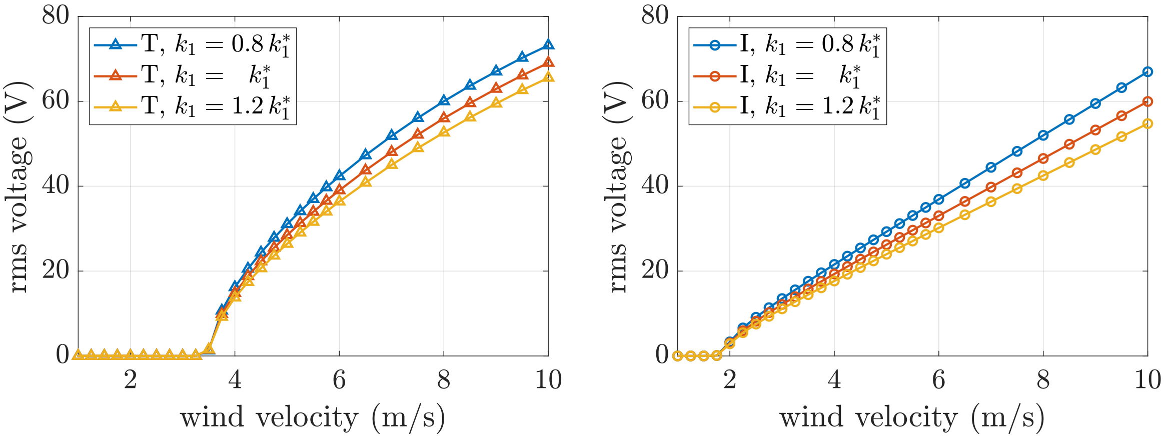

(**a**) (**b**)

Figure 11. Effect of cantilever stiffness on the OC voltage generated by the "T" (**a**) and "I" (**b**) harvesters with fixed tip mass ($M = 0.008$ kg, and corresponding I) and damping coefficient (c_1).

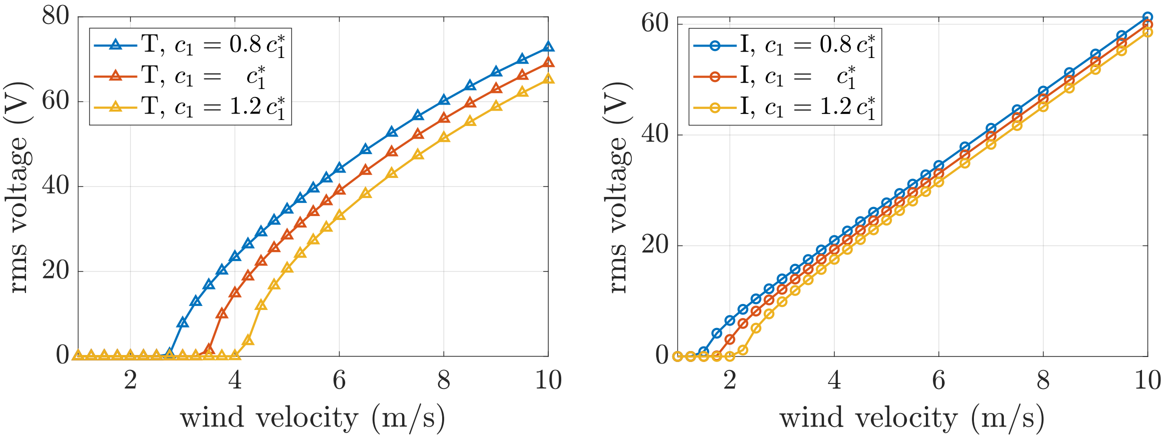

(**a**) (**b**)

Figure 12. Effect of damping on the OCV generated by the "T" (**a**) and "I" (**b**) harvesters with fixed tip mass ($M = 0.008$ kg, and corresponding I) and stiffness (k_1).

6. Energy Extraction from Galloping Piezoelectric Harvester

Piezoelectric energy harvesters excited by wind induced vibrations generate an alternating current (AC) voltage whose amplitude depends on instantaneous mechanical stress. The energy generated by the energy harvester after rectification can be stored in electrostatic form using a supercapacitor [28]. Due to the limited output power, minimization of energy losses in the rectifier becomes a primary requirement. In this work, for ease of implementation, robustness, and improved energy efficiency, a full-bridge rectifier made up of BAT43 Schottky diodes (with low-voltage drop, 0.2 V) was adopted. A supercapacitor with capacitance $C = 500$ mF was chosen for energy storage, considering a target load electrical power of $P_L = 150$ µW. This target represents the power demand of a wireless sensor node for environmental monitoring including microprocessor ESP32 FireBeetle, data logger, sensors, and antenna for data transmission. The maximum power demand is when the sensor is in data-logging and acquired measurements are transmitted to a remote receiver. The current profile of the wireless sensor node is a periodic waveform, with pulsed behavior and average value of $I_L = 40$ µA. Considering a rated voltage of $V_L = 3.3$ V (DC) for sensor electronics, this average current corresponds to the target power ($P_L = V_L\, I_L$).

The proposed experimental conditions were intended to reproduce the operating scenario of a hybrid energy harvesting system, where a photovoltaic panel (with constant DC voltage) acts as a

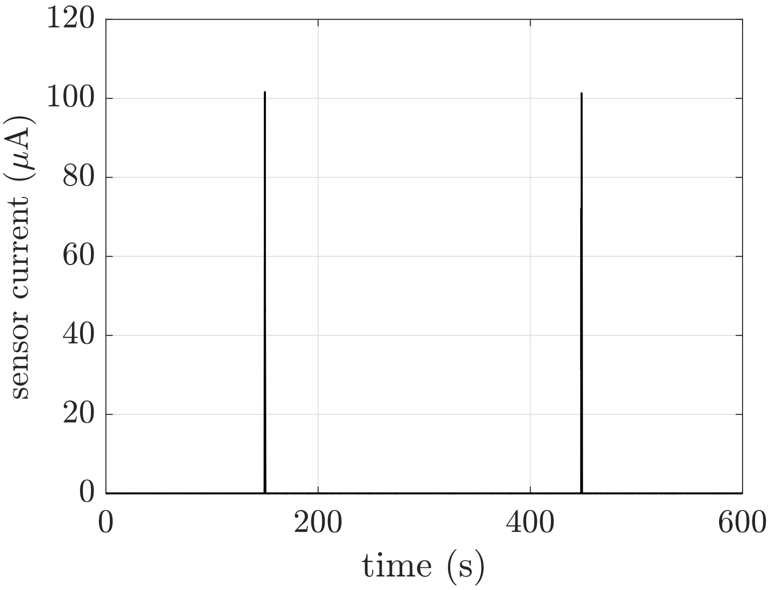

Figure 13. Current waveform of the wireless sensor node during data-logging and data transmission.

primary source and the piezoelectric harvester acts as a complementary source. The DC-DC converter provides a stabilized DC voltage to the electrical load, e.g., a wireless sensor node (Figure 14). In this context, the supercapacitor is assumed to be already pre-charged to a given voltage level; this level affects the output power of the harvester and, in turn, the charging rate of the supercapacitor.

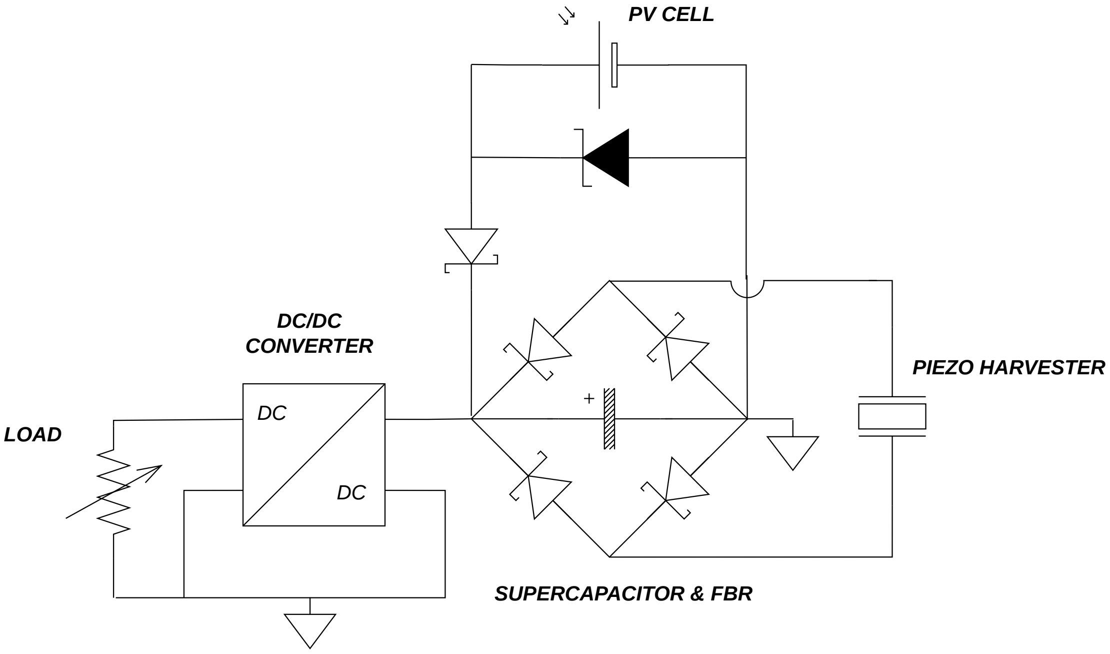

Figure 14. Hybrid energy harvesting (photovoltaic energy production is complemented by piezoelectric harvesting; the supercapacitor SCAP provides an energy buffer for the electrical load).

6.1. Testing of Energy Extraction System

The experimental procedure consisted of the following steps:

- the wind velocity inside the wind tunnel was kept constant at 4 m/s;
- the supercapacitor was pre-charged to a desired voltage level and left in open-circuit conditions for several hours in order to minimize voltage relaxation effects;

- both harvester and capacitor voltages were measured.

Figure 15 shows the schematic of the electric circuit used for the acquisition of voltage signals. The electrical ground reference was set at the negative DC terminal of the rectifier. Consequently, the measured signals were the voltages at the two AC terminals (whose difference corresponds to the piezoelectric output voltage) and the positive DC output voltage. All signals were acquired using a National Instruments NI 9230 data acquisition system (DAQ), which provides four differential input channels.

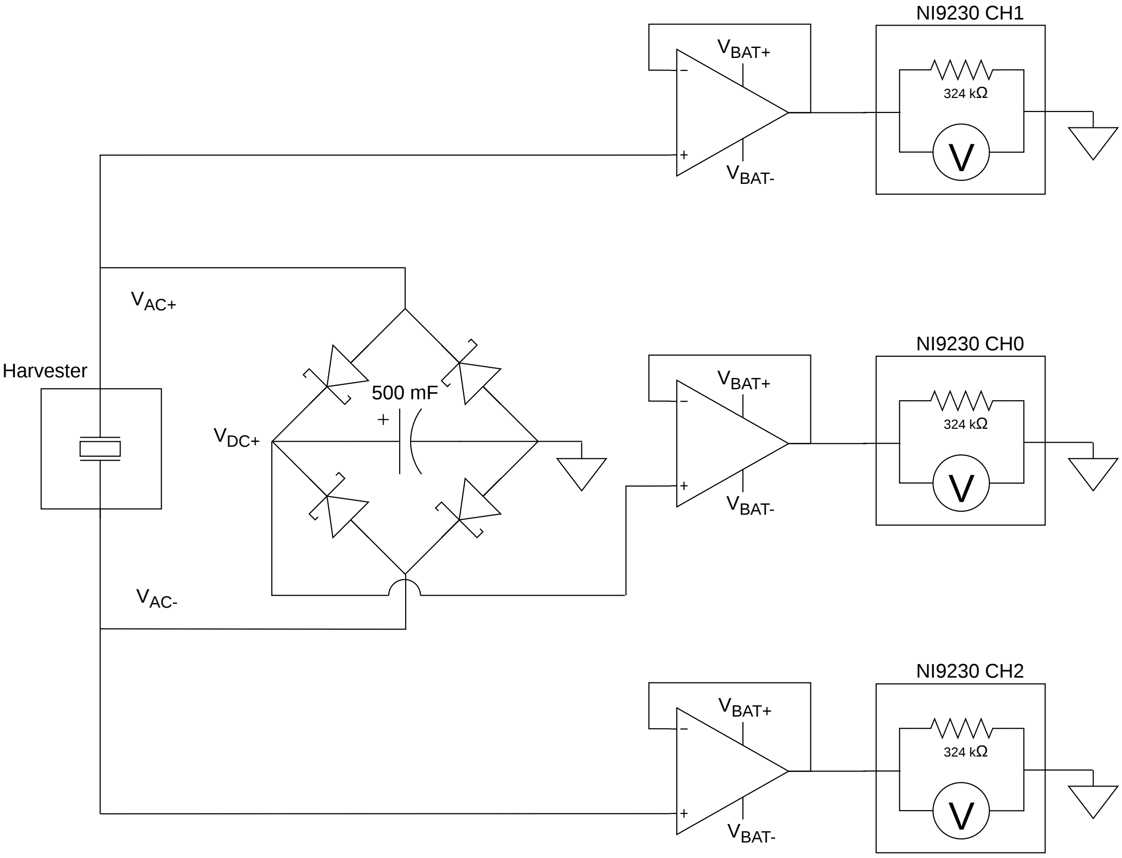

Figure 15. Measurement circuit schematic.

The accurate measurement of the harvester output voltage was particularly challenging due to its high internal impedance, comparable to that of the DAQ input stage. The T-shaped piezoelectric harvester used in the experiments had an internal capacitance $C_p = 43\,\text{nF}$ and the first natural frequency $f_n \approx 18$ Hz, corresponding to an equivalent impedance $Z_{eq} = 1/(2\pi\, f\, C_p) \approx 200\,\text{k}\Omega$. Since the differential input impedance of the DAQ was of the same order of magnitude, a direct electrical connection would significantly load the harvester and perturb its electromechanical behavior. To address this issue, buffer amplifiers were interposed between the harvester and the DAQ channels; these were powered by an external supply. The buffers provided a high input impedance, minimizing the loading effect while preserving the voltage waveforms at the measurement points.

6.2. On Load Voltage Measurements

Figure 16 shows the T-shaped galloping harvester on load voltage, considering an initial capacitor voltage of about 5 V and the above-mentioned experimental conditions. The measurement was carried out for 200 s. It can be observed that the voltage amplitude is influenced by wind turbulence which sometimes causes a sudden decrease, and by the initial capacitor voltage. The maximum amplitude in Figure 16 is attained when the harvester voltage equals the capacitor voltage and there is no conduction

doi:10.20944/preprints202603.0015.v1

through diodes of the full-bridge rectifier. The comparison with the OC voltage generated in the same condition (Figure 17) highlights that the presence of a pre-charged capacitor has a regularizing effect on the harvester voltage waveform.

Figure 18 shows the corresponding voltage of the supercapacitor. The voltage is almost constant (DC) and slightly increases due to the electrical energy provided by the piezoelectric harvester. The amount of stored energy in a time interval $\Delta t = t_2 - t_1 = 200$ s is $W = 1/2\,C\left(v^2(t_2) - v^2(t_1)\right) \approx 40$ mJ, with $v(t_1) = 5.012$ V and $v(t_2) = 5.028$ V, which corresponds to an average power of $P = W/\Delta t = 200$ µW.

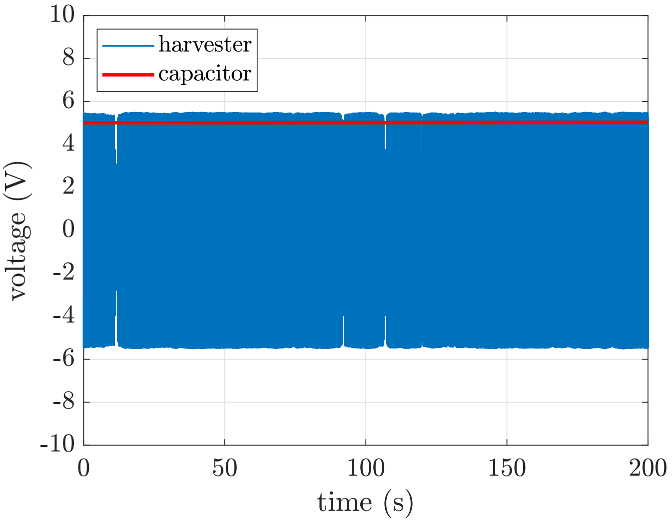

Figure 16. On load voltage generated by the T-shaped harvester ($U = 4$ m/s). Capacitor voltage is depicted as well.

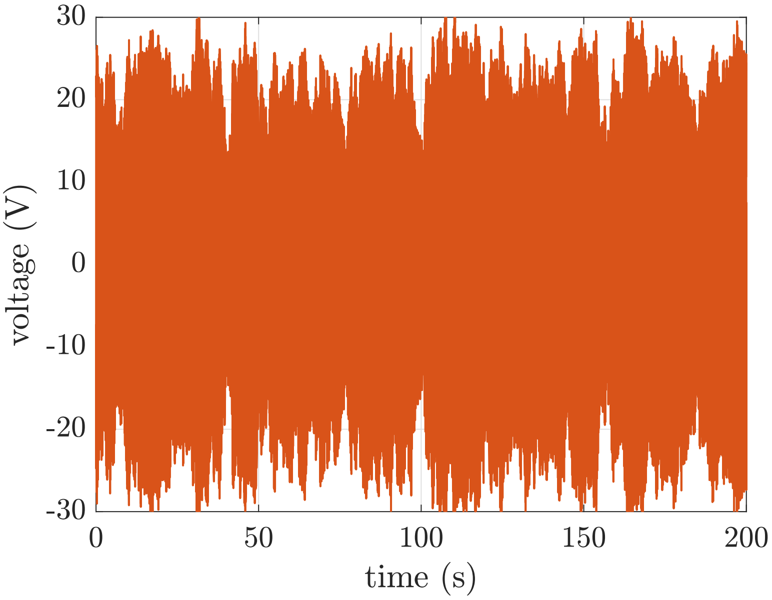

Figure 17. OC voltage generated by the T-shaped harvester ($U = 4$ m/s).

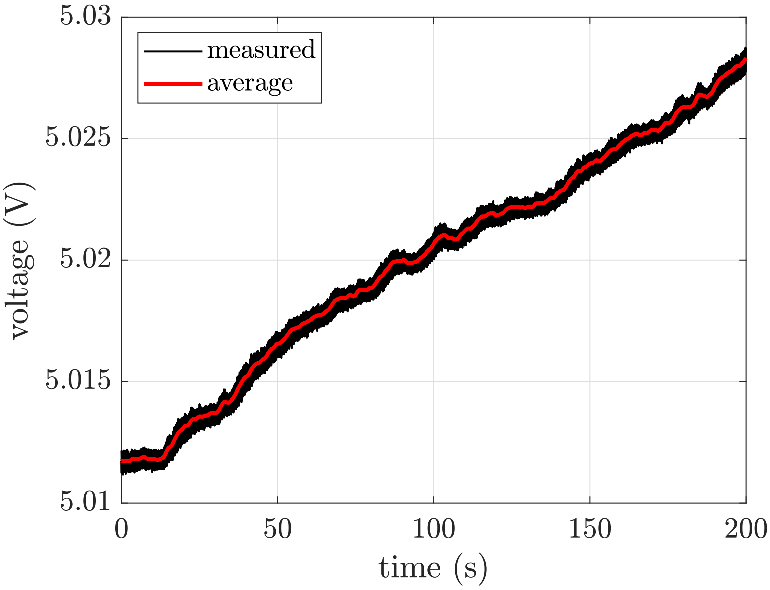

Figure 18. Voltage measured at the supercapacitor terminals.

7. Conclusions

Galloping wind harvesters appear to be well suited to complement solar panels in areas with moderate winds. Experimental tests and numerical simulations reported in this paper show that, adopting the I-configurations, the galloping onset velocity can be moved to the required range of velocity adopting a simple square section bluff-body.

The multiphysics harvester model takes into account vibratory, fluid dynamic, and piezoelectric phenomena and is suited to both T-shaped and I-shaped harvesters. After a proper tuning by means of experimental tests, it can simulate the behavior of the harvester with good accuracy and extend the range of investigation.

Experimental tests on a galloping harvester equipped with a rectifier and a supercapacitor showed that the harvester is able to supply a wireless sensor node without need of a battery. Future work will deal with the integration of converter model with the harvester model. Simulations will be carried out to analyze the performance of bluff-bodies with different cross sections and to verify the possibility of scaling up the sizes of the I-shaped harvester, in order to obtain larger powers.

Author Contributions: Conceptualization, A.P., G.F., M.T., M.Be., M.B., D.D., F.M, and A.D.; methodology, A.P., G.F., M.T., and A.D.; software, A.P. and M.T.; validation, A.P., G.F., M.T, and M.B.; Formal Analysis, A.P., G.F., M.T., M.B., F.M, and A.D.; investigation, M.B., and G.F.; Data Curation, M.Be., M.B., D.D., F.M, and A.D.; writing—original draft preparation, A.P., G.F., M.T., M.Be., M.B., D.D., F.M. and A.D.; writing—review and editing, F.M; supervision, F.M, A.D. All authors have read and agreed to the published version of the manuscript.

Funding: This research was funded by the Department of Industrial Engineering, University of Padova, grant no. C93C24006490005 (Project SID 2024 RaWiHaS).

Institutional Review Board Statement: Not applicable.

Informed Consent Statement: Not applicable.

Data Availability Statement: Not applicable.

Conflicts of Interest: The authors declare no conflict of interest.

References

1. Liu, L.; Guo, X.; Lee, C. Promoting smart cities into the 5G era with multi-field Internet of Things (IoT) applications powered with advanced mechanical energy harvesters. *Nano Energy* **2021**, *88*. https://doi.org/10.1016/j.nanoen.2021.106304.

2. Zhao, L.; Yang, Y. Toward Small-Scale Wind Energy Harvesting: Design, Enhancement, Performance Comparison, and Applicability. *Shock and Vibration* **2017**, *2017*. https://doi.org/10.1155/2017/3585972.
3. Lu, C.; Jiang, X.; Li, L.; Zhou, H.; Yang, A.; Xin, M.; Fu, G.; Wang, X. Wind energy harvester using piezoelectric materials. *Review of Scientific Instruments* **2022**, *93*. https://doi.org/10.1063/5.0065462.
4. Doria, A.; Fanti, G.; Filipi, G.; Moro, F. Development of a novel piezoelectric harvester excited by raindrops. *Sensors (Switzerland)* **2019**. https://doi.org/10.3390/s19173653.
5. Palomba, I.; Tonan, M.; Doria, A. Design of cantilever harvesters excited by raindrop impacts. *Mechanical Systems and Signal Processing* **2025**, *225*, 112284. https://doi.org/10.1016/j.ymssp.2024.112284.
6. Pasetto, A.; Tonan, M.; Moro, F.; Doria, A. Design Parameters Affecting the Performance of Vortex-Induced Vibration Harvesters. *Micromachines* **2025**, *16*. https://doi.org/10.3390/mi16020122.
7. Tonan, M.; Palomba, I.; Pasetto, A.; Doria, A. Interaction between vortex-induced vibrations and base vibrations in piezoelectric harvesters. *International Journal of Mechanical System Dynamics*. To appear., https://doi.org/10.1002/msd2.70054.
8. Barrero-Gil, A.; Alonso, G.; Sanz-Andres, A. Energy harvesting from transverse galloping. *Journal of Sound and Vibration* **2010**, *329*, 2873–2883. https://doi.org/10.1016/j.jsv.2010.01.028.
9. Yan, Z.; Abdelkefi, A.; Hajj, M.R. Piezoelectric energy harvesting from hybrid vibrations. *Smart Materials and Structures* **2014**, *23*. https://doi.org/10.1088/0964-1726/23/2/025026.
10. Erturk, A.; Vieira, W.; De Marqui Jr., C.; Inman, D. On the energy harvesting potential of piezoaeroelastic systems. *Applied Physics Letters* **2010**, *96*. https://doi.org/10.1063/1.3427405.
11. Orrego, S.; Shoele, K.; Ruas, A.; Doran, K.; Caggiano, B.; Mittal, R.; Kang, S. Harvesting ambient wind energy with an inverted piezoelectric flag. *Applied Energy* **2017**. https://doi.org/10.1016/j.apenergy.2017.03.016.
12. Akaydin, H.D.; Elvin, N.; Andreopoulos, Y. Experimental study of a self-excited piezoelectric energy harvester. 2010, Vol. 1, *ASME 2010 Conference on Smart Materials, Adaptive Structures and Intelligent Systems, SMASIS 2010*, p. 179 – 185. https://doi.org/10.1115/SMASIS2010-3729.
13. Akaydin, H.; Elvin, N.; Andreopoulos, Y. The performance of a self-excited fluidic energy harvester. *Smart Materials and Structures* **2012**. https://doi.org/10.1088/0964-1726/21/2/025007.
14. Bernitsas, M.M.; Raghavan, K.; Ben-Simon, Y.; Garcia, E.M. VIVACE (Vortex Induced Vibration Aquatic Clean Energy): A new concept in generation of clean and renewable energy from fluid flow. *Journal of Offshore Mechanics and Arctic Engineering* **2008**, *130*. https://doi.org/10.1115/1.2957913.
15. Mehmood, A.; Abdelkefi, A.; Hajj, M.; Nayfeh, A.; Akhtar, I.; Nuhait, A. Piezoelectric energy harvesting from vortex-induced vibrations of circular cylinder. *Journal of Sound and Vibration* **2013**, *332*, 4656 – 4667.
16. Zhao, L.; Tang, L.; Yang, Y. Small wind energy harvesting from galloping using piezoelectric materials. 2012, Vol. 2, pp. 919 – 927. https://doi.org/10.1115/SMASIS2012-8212.
17. Tan, T.; Zuo, L.; Yan, Z. Environment coupled piezoelectric galloping wind energy harvesting. *Sensors and Actuators A Physical* **2021**, *323*. https://doi.org/10.1016/j.sna.2021.112641.
18. Li, Z.; Zhou, S.; Yang, Z. Recent progress on flutter-based wind energy harvesting. *International Journal of Mechanical System Dynamics* **2022**, *2*, 82 – 98. https://doi.org/10.1002/msd2.12035.
19. Choi, C.K.; Kwon, D.K. Wind tunnel blockage effects on aerodynamic behavior of bluff body. *Wind and Structures An International Journal* **1998**, *1*, 351–364. https://doi.org/10.12989/was.1998.1.4.351.
20. Morse, T.; Govardhan, R.; Williamson, C. The effect of end conditions on the vortex-induced vibration of cylinders. *Journal of Fluids and Structures* **2008**, *24*, 1227–1239. Unsteady Separated Flows and their Control, https://doi.org/10.1016/j.jfluidstructs.2008.06.004.
21. Blevins, R.D. *Flow-induced vibration*; Van Nostrand Reinhold Company, 1977.
22. Facchinetti, M.; de Langre, E.; Biolley, F. Coupling of structure and wake oscillators in vortex-induced vibrations. *Journal of Fluids and Structures* **2004**, *19*, 123 – 140. https://doi.org/10.1016/j.jfluidstructs.2003.12.004.
23. Zhao, D.; Hu, X.; Tan, T.; Yan, Z.; Zhang, W. Piezoelectric galloping energy harvesting enhanced by topological equivalent aerodynamic design. *Energy Conversion and Management* **2020**. https://doi.org/10.1016/j.enconman.2020.113260.
24. Tian, H.; Shan, X.; Cao, H.; Song, R.; Xie, T. A method for investigating aerodynamic load models of piezoaeroelastic energy harvester. *Journal of Sound and Vibration* **2021**, *502*. https://doi.org/10.1016/j.jsv.2021.116084.
25. Tamimi, V.; Wu, J.; Esfehani, M.J.; Zeinoddini, M.; Naeeni, S.T.O. Comparison of hydrokinetic energy harvesting performance of a fluttering hydrofoil against other Flow-Induced Vibration (FIV) mechanisms. *Renewable Energy* **2022**, *186*, 157 – 172. https://doi.org/10.1016/j.renene.2021.12.127.

26. Bibo, A.; Daqaq, M.F. Energy harvesting under combined aerodynamic and base excitations. *Journal of Sound and Vibration* **2013**, *332*, 5086 – 5102. https://doi.org/10.1016/j.jsv.2013.04.009.
27. Priya, S.; Inman, D. *Energy harvesting technologies*; Springer New York, NY, 2009; pp. 1–517. https://doi.org/10.1007/978-0-387-76464-1.
28. Dicken, J.; Mitcheson, P.D.; Stoianov, I.; Yeatman, E.M. Power-extraction circuits for piezoelectric energy harvesters in miniature and low-power applications. *IEEE Transactions on power electronics* **2012**, *27*, 4514–4529. https://doi.org/10.1109/TPEL.2012.2192291.